

In vivo stiffness of multiple sclerosis lesions is similar to that of normal-appearing white matter

Helge Herthum, Stefan Hetzer, Michael Scheel, Mehrgan Shahryari, Jürgen Braun, Friedemann Paul, Ingolf Sack

Document type

Postprint (accepted version)

This version is available at

<https://doi.org/10.17169/refubium-32404>

Citation details

Herthum H, Hetzer S, Scheel M, Shahryari M, Braun J, Paul F, et al. In vivo stiffness of multiple sclerosis lesions is similar to that of normal-appearing white matter. *Acta Biomaterialia*. Elsevier BV; 2022. p. 410–421. DOI: 10.1016/j.actbio.2021.10.038

Terms of use

This work is licensed under a Creative Commons Attribution-NonCommercial-NoDerivatives 4.0 International license: <https://creativecommons.org/licenses/by-nc-nd/4.0/>

In vivo stiffness of multiple sclerosis lesions is similar to that of normal-appearing white matter.

Helge Herthum¹, Stefan Hetzer², Michael Scheel^{3,4}, Mehrgan Shahryari⁵, Jürgen Braun¹, Friedemann Paul^{3,6,7}, Ingolf Sack^{5,*}

¹Institute of Medical Informatics, Charité – Universitätsmedizin Berlin, Corporate Member of Freie Universität Berlin, Humboldt-Universität zu Berlin, and Berlin Institute of Health, 10117, Berlin, Germany

²Berlin Center for Advanced Neuroimaging (BCAN), 10117, Berlin, Germany

³NeuroCure Clinical Research Center, Charité - Universitätsmedizin Berlin, Corporate Member of Freie Universität Berlin, Humboldt-Universität zu Berlin, and Berlin Institute of Health, 10117, Berlin, Germany.

⁴Department of Neuroradiology, Charité - Universitätsmedizin Berlin, Corporate Member of Freie Universität Berlin, Humboldt-Universität zu Berlin, and Berlin Institute of Health, 10117, Berlin, Germany

⁵Department of Radiology, Charité – Universitätsmedizin Berlin, Corporate Member of Freie Universität Berlin, Humboldt-Universität zu Berlin, and Berlin Institute of Health, 10117, Berlin, Germany

⁶Max Delbrück Center for Molecular Medicine and Charité - Universitätsmedizin Berlin, Corporate Member of Freie Universität Berlin, Humboldt-Universität zu Berlin, and Berlin Institute of Health, Experimental and Clinical Research Center, 13125, Berlin, Germany

⁷Department of Neurology, Charité - Universitätsmedizin Berlin, Corporate Member of Freie Universität Berlin, Humboldt-Universität zu Berlin, and Berlin Institute of Health, 10117, Berlin, Germany.

***Corresponding author:**

Ingolf Sack, PhD

Department of Radiology

Charité – Universitätsmedizin Berlin

Charitéplatz 1

10117 Berlin, Germany

Tel +49 30 450 539058

Ingolf.sack@charite.de

Abstract

In 1868, French neurologist Jean-Martin Charcot coined the term multiple sclerosis (MS) after his observation that numerous white matter (WM) glial scars felt like sclerotic tissue. Nowadays, magnetic resonance elastography (MRE) can generate images with contrast of stiffness (CS) in soft in vivo tissues and may therefore be sensitive to MS lesions, provided that sclerosis is indeed a mechanical signature of this disease.

We analyzed CS in a total of 147 lesions in patients with relapsing-remitting MS, compared with control regions in contralateral brain regions, and phantom data as well as performed numerical simulations to determine the delineation limits of multifrequency MRE (20-40Hz) in MS.

MRE analysis of simulated waves revealed a delineation limit of approximately 10% CS for detecting 9-mm lesions (mean size in our patient population). Due to inversion bias, this limit is reached when true CS is -11% for soft and 35% for stiff lesions. In vivo MRE identified 35 stiffer lesions and 17 softer lesions compared with surrounding WM (mean stiffness: 934 ± 82 Pa). However, a similar pattern was found in the contralateral brain, suggesting that the range of stiffness changes in WM lesions due to MS is within the normal range of WM variability and normal heterogeneity-related CS.

Consequently, Charcot's original intuition that MS is a focal sclerotic disease can neither be dismissed nor confirmed by in vivo MRE. However, the observation that MS lesions do not markedly differ in stiffness from surrounding brain tissue suggests that marked tissue sclerosis is not a mechanical signature of MS.

Statement of Significance

Multiple sclerosis (MS) was named by J.M. Charcot after the sclerotic changes in brain tissue he found in post-mortem autopsies. Since then, nothing has been revealed about the actual stiffening of MS lesions in vivo. Studying the viscoelastic properties of plaques in their natural environment is a major challenge that can only be overcome by MR elastography (MRE). Therefore, we used multifrequency MRE to answer the question whether MS lesions in patients with a relapsing-remitting disease course are mechanically

different than surrounding tissue. Our findings suggest that the range of stiffness changes in white matter lesions due to MS is within the normal range of white matter variability and in vivo tissue sclerosis might not be a mechanical signature of MS.

Keywords: multifrequency MRE; viscoelasticity; brain; Multiple sclerosis

Introduction

More than a hundred and fifty years ago, Jean-Martin Charcot reported *sclérose en plaques* as a new neurological disease, which later became known as multiple sclerosis (MS) in the English literature [1]. The pathologic hallmark of MS is multiple focal areas of myelin loss within the central nervous system (CNS) known as plaques or lesions. As such plaques progress from acutely active to chronically inactive, astrocytes produce glial fibers that form a glial scar within the demyelinated plaques. It seems plausible that these characteristics of chronic MS lesions contribute to a firmer material behavior compared to normal white matter.

However, there are also arguments that question whether MS is predominantly characterized by tissue sclerosis: First, acute demyelinated lesions have been reported to be softer than healthy tissue [2], which is in agreement with the marked softening of CNS tissue observed after injury [3]. Second, these reports are all based on excised *ex vivo* tissue slices, either fixed by aldehyde and cryosectioned [2] or submerged in cooled liquid for substitution of blood and cerebrospinal fluid (CSF) and glued to sample holders [3]. Magnetic resonance elastography (MRE) has shown that freezing and thawing of biological tissues induces cell disruption, leading to markedly lower shear modulus values [4]. In addition, MRE showed, that blood perfusion and intracranial pressure critically influence brain stiffness [5-8], and that brain tissue stiffens post mortem [9, 10]. Furthermore, *in vivo* MRE of the human brain [11-13] has revealed disseminated tissue softening due to MS [14], both in early phases of the disease [15] and, with increased effect size, in chronic MS [16, 17]. Similar patterns of brain softening were observed in mouse models of demyelination [18] and experimental autoimmune encephalitis [19-22].

In contrast to these remarkably consistent MRE reports of large-scale brain softening, there are only limited systematic data on focal MS lesions in the literature [23, 24]. Possible reasons are the variability of MRE stiffness in normal-appearing white matter (NAWM [25]), which is on the order of 10% [26-29], as well as technical limitations regarding the consistency of MRE stiffness values in small lesions [30-32].

Therefore, we here address the delineation of MS lesions by current multifrequency MRE considering lesion size, stiffness contrast and the variability of surrounding NAWM stiffness. Using 2D simulations we investigate how stiffness estimates are biased by focal lesion size and stiffness contrast. This was further analyzed by MRE phantom experiments. To stabilize our wave field analysis and support inverse problem solutions, we use multifrequency-multicomponent inversion techniques based on direct inversion [33] and wavenumber recovery [34]. While the two methods differ fundamentally in their physical approaches, both have been previously used in brain MRE [7, 35]. It remains to be established which of the two inversion techniques is best suited for delineation of MS lesions, hence we use both methods in parallel. We apply the two inversion techniques to the brains of twelve patients with previously identified MS lesions to analyze their representation in MRE maps in comparison with control regions of similar sizes in matched locations in the contralateral brain.

Our aim is to answer the question whether MS lesions in patients with a relapsing-remitting disease course are significantly softer or stiffer than surrounding tissue.

Methods

Subjects

Twelve patients with relapsing-remitting MS (5 women; mean age \pm SD: 45 \pm 14 years, age range: 22 to 62 years) were investigated in this study. All patients were stable RRMS patients (i.e., no relapse within one month prior to MRI) and were on standard immunomodulatory treatment (glatiramer acetate, dimethyl fumarate, teriflunomide, fingolimod or natalizumab).

All patients underwent both standard clinical magnetic resonance imaging (MRI) and multifrequency MRE. Patient demographics and disease data are given in Table 1.

The study was approved by the ethics committee of Charité – Universitätsmedizin Berlin in accordance with the Ethical Principles for Medical Research Involving Human Subjects of the World Medical Association Declaration of Helsinki. All patients gave informed written consent prior to the imaging examination.

Standard clinical MRI

All experiments were performed in a 3T MRI scanner (Siemens PRISMA, Erlangen, Germany) equipped with a 32-channel head coil. For all pulse sequences, the slices were automatically positioned using the scanner's auto align function based on the localizer images to ensure centered images with optimal, anatomical left-right laterality. No further 3D translation or rotation of the images was necessary. T2-weighted imaging was performed with a single-slab 3D turbo-spin-echo (TSE) sequence, which was combined with fluid attenuation inversion recovery (FLAIR; TE 388 ms, TR 6000 ms, TI 2100 ms, ETL 251 ms).

MRE experimental setup

Multifrequency MRE using a single-shot, spin-echo echo-planar imaging (EPI) sequence was performed. Eight phase offsets equally spaced over a vibration period were recorded for 36 axial slices with harmonic vibrations induced at 20, 25, 30 and 40 Hz using pressurized air drivers as described elsewhere [36]. Further imaging parameters were: field of view 200 x 200 mm², voxel size 2 x 2 x 2 mm³, TE 78 ms, TR 4680 ms, 34 mT/m amplitude of the motion-encoding gradient with first order moment nulling. Encoding efficiencies were 8.6, 6.4, 5.4, and 5.3 $\mu\text{m}/\text{rad}$ for 20, 25, 30, and 40 Hz, respectively, similar to previously reported results [37, 38]. Total acquisition time for a full set of 3D multifrequency MRE data was approximately 8 min.

Registration and segmentation

Complex MRE images were corrected in a slice-wise fashion (2D) for stochastic head motion in the range of ± 2 mm using SPM12 [39]. Mean MRE magnitude images were calculated by averaging over the frequencies, encoding directions, and time steps. FLAIR images were co-registered to the mean MRE magnitude images using SPM12.

3D lesions with a minimum size of 32 mm³ were manually identified and demarcated using ITK-SNAP [40] based on mean MRE magnitude images by an experienced neuroradiologist (MS) with more than 10 years of experience in MS lesion detection. The co-registered FLAIR images were used for visual guidance in delineating MS lesions.

Direct segmentation based on FLAIR images was precluded by slight co-registration imperfections related to blurring, susceptibility artifacts, and image distortions. For the same reason, mean MRE images and stiffness maps were not normalized to the MNI space. Automatic segmentation of white matter, gray matter, and cerebrospinal fluid (CSF) was done based on mean MRE magnitude images using SPM12. Lesions which were falsely segmented as CSF were corrected using the manually segmented lesion masks. Tissue probability maps were converted to logical masks using a threshold of 0.5.

MRE data analysis

Two independent multifrequency inversion methods were applied in this study: multifrequency dual elasto-visco (MDEV) inversion as an established method [28, 41] and wavenumber-based (k-)MDEV inversion [34] as a novel method for the brain. MDEV can generate high-resolution maps of magnitude shear modulus ($|G^*|$ in Pa) but suffers from noise in tissues with a low signal-to-noise ratio (SNR) due to second-order derivative operators [42]. k-MDEV recovers shear wave speed (SWS in m/s) by noise-robust first-order derivatives but needed modification in order to account for the higher SNR and larger heterogeneity in brain scans compared with abdominal applications [35], which still represents the standard application area of k-MDEV [43-45]. Both processing pipelines are publicly available at <https://bioqic-apps.charite.de/> [46] and are further detailed in the following.

MDEV

Complex MR images were smoothed using a 2-dimensional (2D) Gaussian filter with 5-pixel kernel size and standard deviation of 0.65 pixels. Then, phase images were unwrapped and high-pass-filtered using in-plane, symmetric, first-order, finite-difference operators of 3-pixel stencil size [47]. Temporal Fourier transformation was then applied to retrieve motion at driving frequency. The resulting complex-valued wave images were smoothed by a 2D Butterworth low-pass filter with 100 m^{-1} threshold and processed by 2D MDEV inversion as previously described and applied to MRE data [48].

k-MDEV

k-MDEV, which was originally proposed for abdominal MRE by Tzschätzsch *et al.*[34], was adapted to the brain as outlined in the supplementary material of [35]. Therefore, prior to unwrapping of phase images, a Butterworth low-pass filter of order 3 and threshold 250 m^{-1} was used for noise suppression. In addition to directional filtering, a radial bandpass Butterworth filter of third order with a high-pass threshold of 15 m^{-1} and low-pass threshold of 200 m^{-1} was used for elimination of compression waves and additional noise suppression. All frequency components of the wave fields were weighted equally in the 2D inversion. For comparison with $|G^*|$, SWS was converted to shear modulus by applying the elastic model, i.e., $|G^*|_{\text{SWS}} = \text{SWS}^2 \cdot \rho$, with density $\rho = 1000 \text{ kg/m}^3$.

Lesion contrast quantification

Lesion contrast for $|G^*|$, $|G^*|_{\text{SWS}}$ and T2-weighted FLAIR intensity ($T2_{\text{int}}$) was defined as:

$$\text{contrast} = \frac{\text{mean}(\text{lesion tissue}) - \text{mean}(\text{surrounding tissue})}{\text{mean}(\text{surrounding tissue})}.$$

Mean(lesion tissue) and *mean(surrounding tissue)* were obtained by averaging signal intensity and stiffness parameters within regions of interest (ROIs) of MS lesions (corresponding to the prescribed lesion masks) and automatically generated masks of tissue surrounding each lesion ROI. A surrounding tissue mask consisted of a ring of one voxel thickness at a distance of two voxels from the lesion mask. CSF and other lesions as well as solid-fluid interfaces, as identified by $|G^*|$ values below 550 Pa, were automatically excluded from the surrounding tissue ROI [29, 49, 50]. To test if the contrast reflects intrinsic lesion properties or normal brain heterogeneity, we flipped all lesion masks to the contralateral hemisphere of the centered MRE magnitude images and repeated the evaluation in these control regions. Again, CSF, other lesions and solid-fluid tissue boundaries were excluded so that control regions were located in NAWM. As a result of this exclusion procedure, the size of the masks for some control regions was reduced. The contrast of control regions relative to their surrounding tissue was then calculated in the same way as that of MS lesions. In addition, we compared the stiffness

and FLAIR intensity of MS lesions with their control regions. Overall, three contrasts were analyzed:

C1: Manually delineated MS lesion tissue versus automatically selected surrounding NAWM.

C2: NAWM control region (MS lesions flipped to the contralateral side) versus automatically selected surrounding NAWM.

C3: Manually delineated MS lesion versus control region in the contralateral hemisphere.

Representative masks of delineated MS lesions (red) and surrounding tissue (green) are shown in Figure 1. Additionally, automatically generated control regions (blue) in the contralateral NAWM and their surrounding tissue (yellow) are shown.

We also selected control regions of the same size and number as the MS lesions in each patient but placed them randomly in the slice matched NAWM. Nevertheless, this random reference yielded similar results as C2 and C3 and was henceforth not used. To further investigate the effects of the proximity of MS lesions to CSF, we consecutively enlarged the CSF mask by 1, 2, 3 ...6 voxels and determined which of the MS lesions overlapped at least 30% with the enlarged CSF masks. These MS lesions were then assigned to subgroups of different proximities of 1 to 6 voxels to CSF.

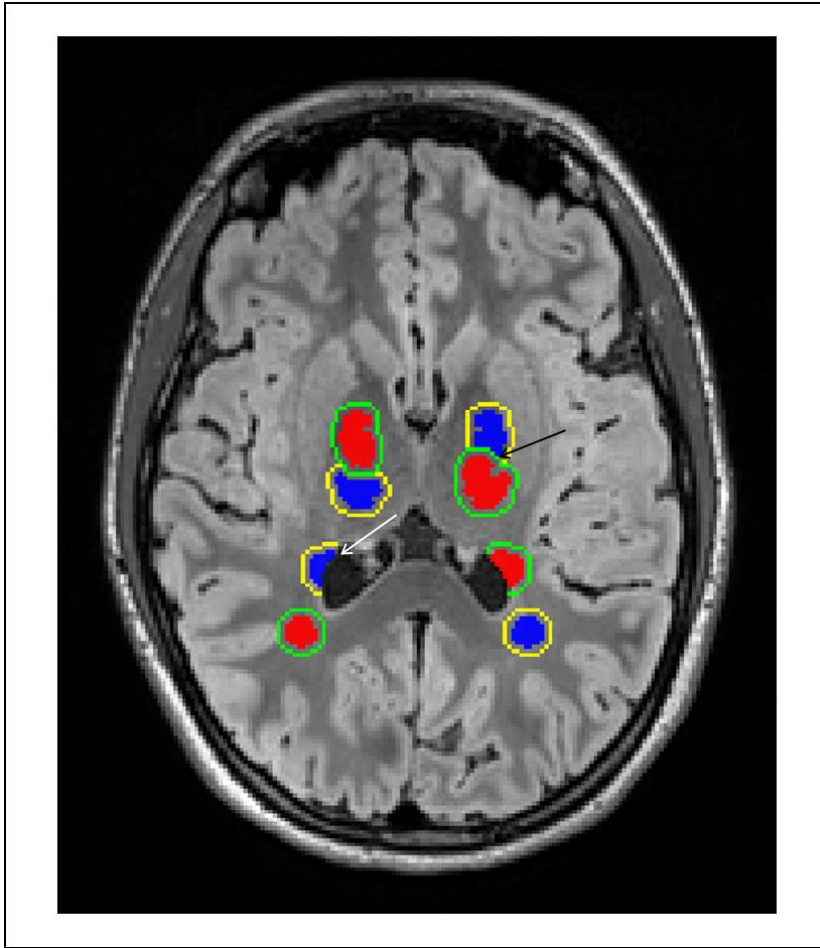


Figure 1: Illustration of masking MS lesions (red), surrounding NAWM (green), control regions in the contralateral hemisphere (blue), and NAWM surrounding control regions (yellow) superimposed on a FLAIR image. Regions of CSF were automatically subtracted from all masks while regions of MS lesions were subtracted from control regions. The black arrow indicates an area where a control region overlaps with an MS lesion. The white arrow indicates an area where a control region falls into CSF, causing the size of the control region to be automatically decreased.

Wave simulations

Wave simulations were used to estimate sensitivity limits of MDEV and k-MDEV to lesions. Therefore, we used the Matlab code (the Mathworks Inc. Natick, MN, USA) for 2D finite-difference wave simulations as a plane-stress formulation with Sommerfeld boundary conditions presented in [11] (chapter 8, *Numerical Methods and*

Postprocessing). The three different components of the wave fields at four frequencies (20, 25, 30, 40 Hz) were simulated by different force terms corresponding to wave stimulations at different sites. Left-right deflections were mimicked by a plane source along the top row, up-down deflections by a plane source along the left column, and through-plane deflections by a phase shifted combination of left-right and up-down source terms. The matrix size was 80 x 80 pixels with 2-mm edge size. Complex-valued Gaussian noise of $\sigma = 0.02$ was added to mimic our in vivo scenario of displacement SNR of approximately 29 dB according to Donoho *et al.* [51] and outlined further below. Note that the Donoho method accounts for non-Gaussian noise based on wavelet decomposition, which prevents a direct translation of simulated (Gaussian) SNR to in vivo SNR. Background $|G^*|$ was set to 1.5 kPa as reported previously [29] while lesions were simulated by circular inclusions with Gaussian stiffness profile of varying sizes and stiffness values. The size was varied from 5 mm to 38 mm in steps of 0.65 mm, while lesion $|G^*|$ contrast was varied from -75% to +200% in steps of 5.5% relative to a background $|G^*|$ of 1.5 kPa. The complex-valued wave images were used as input for MDEV and k-MDEV using the same preprocessing procedure as for in vivo analysis.

Again, the contrast of the inclusion relative to the background stiffness was determined and compared with the underlying true contrast of the simulation to generate an error map depending on size and true contrast of the inclusion.

The delineation limit was defined using a series of simulation-based, noisy $|G^*|$ and $|G^*|_{\text{sws}}$ maps of 9-mm inclusions with stiffness contrasts varied between -80% and 80% in steps of 2%. Noise was added to the simulated waves prior to the postprocessing with MDEV and k-MDEV to resemble the in vivo scenario of 29 dB SNR. The position of the inclusions was known, and the experienced observer had to indicate at what contrast the inclusion became visually apparent similar to the procedure described in [31]. Example $|G^*|$ contrast maps at different percentages are shown in Figure 2a.

Phantom experiment

For further validation we used MRE phantom data published by Papazoglou *et al.* [41] and Tzschätzsch *et al.* [34], which are publicly available at <https://bioqic-apps.charite.de/>. The

phantom was made of agar-based Wirogel (Bego Inc., Bremen, Germany) with four parallel cylindrical inclusions of 11-mm diameter with $|G^*|$ contrasts of +248%, -51%, -44% and +43% relative to a gel matrix of $|G^*|_{\text{matrix}} = 10$ kPa. As described in [41], ground-truth values were determined by rheometry and parameter fits based on the spring-pot model for frequencies between 30 and 100 Hz in steps of 10 Hz. A power law exponent α of only 0.03 reported in [41] indicates that there is almost no frequency dispersion of viscoelastic parameters. Henceforth, phantom ground-truth $|G^*|$ values were averaged over the same frequencies as used for the MRE experiments of the phantom (30 – 100 Hz). Wave images were analyzed by the same inversion methods explained above. As for in vivo data, a mask with a distance of two voxels from the inclusion and one voxel thickness was automatically generated and taken as the surrounding tissue ROI. The simulated contrast and the respective error compared to the true contrast were determined.

SNR analysis

Wave displacement signal-to-noise ratio (SNR) for the phantom and in vivo experiments was derived using the blind noise estimation method proposed by Donoho *et al.* [51], which was previously applied to MRE data [50, 52, 53]. The underlying wavelet analysis is well suited for the differentiation of spatial frequencies of harmonic waves and noise in MRE [54]. SNR was determined for the phantom matrix and inclusions as well as for in vivo NAWM and each MS lesion.

Statistical tests

A one-sided paired Welch's t-test was conducted to compare the size of manually delineated MS lesion masks with that of the automatically generated contralateral control region masks. In addition, Cohen's d was calculated to estimate the size of the effect. Correlation analyses were performed between stiffness contrast C1 and lesion SNR, size and CSF proximity using Pearson's correlation coefficient. P-values were corrected for multiple comparisons using the Bonferroni method (adjusted p^*). To test for significant differences in contrasts C1, C2 and C3 based on $|G^*|$, $|G^*|_{\text{SWS}}$, and $T2_{\text{int}}$, a linear mixed-effects model with varying intercept was employed. Contrasts were used as dependent

variable and the lesion type (MS lesion or control region) as independent variable. Subjects and lesion numbers were assigned as random effects. All statistical analysis was done in R (version 4.0.2). P-values below 0.05 were considered statistically significant.

Results

Wave simulations

Figure 2a shows a series of simulation-based $|G^*|$ maps with decreasing negative contrast to illustrate the delineation limit of approximately 10% for a 9-mm lesion and noise levels similar to in vivo data. Since the ground-truth $|G^*|$ contrast was chosen to achieve the desired stiffness contrast, the delineation limit result was independent of the positive or negative stiffness contrast and the type of inversion. In addition the simulation results are given for two different inclusion sizes of 1 cm (top row) and 2 cm (middle row) with -80% contrast in (b) and +80% contrast in (c), both derived from the simulated wave fields with a displacement SNR of 29 dB (bottom row). Wave field components were left-right, top-bottom and through-plane as indicated in the figure for 30 Hz vibration frequency. The top row shows stiffness contrast images in $|G^*|$ in % for ground-truth, MDEV $|G^*|$ and k-MDEV $|G^*|_{\text{sws}}$. The second row shows $|G^*|$ and $|G^*|_{\text{sws}}$ as absolute values. Overall, MDEV was apparently better at reconstructing the shape of the inclusion, albeit with higher noise levels than k-MDEV. k-MDEV-based $|G^*|_{\text{sws}}$ maps suffer from low frequency spatial variations. Both methods were more sensitive to a negative stiffness contrast than to a positive contrast.

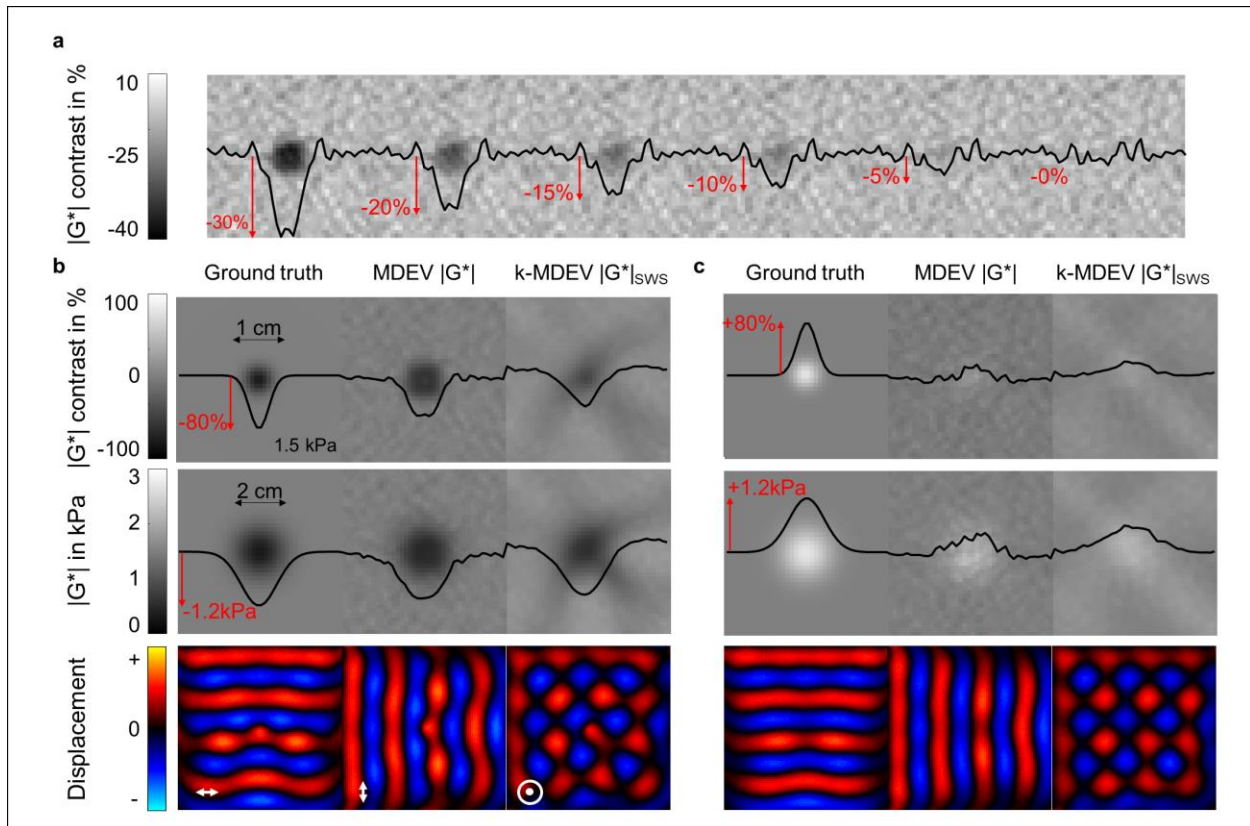


Figure 2: Illustration of lesion delineation by MRE of simulated waves. **a)** $|G^*|$ contrast maps of a soft inclusion of 9 mm size for illustrating the visual delineation limit of -10%. Ground-truth stiffness was adapted to provide stiffness contrast between 0% and -30% after wave processing with MDEV **b)** Results for a soft inclusion with -80% contrast. Shown are stiffness contrast images of $|G^*|$ and $|G^*|_{\text{SWS}}$ for two different inclusion sizes of 1 cm in the top row and 2 cm in the middle row (absolute stiffness values $|G^*|$ and $|G^*|_{\text{SWS}}$ in kPa). The three simulated wave field components for 30 Hz vibration frequency are shown in the bottom row (\leftrightarrow , \updownarrow , \odot denote deflections left-right, up-down [anterior-posterior] and through-plane [head-to-feet], respectively). **c)** Results for a stiff inclusion with +80% contrast. Red arrows indicate peak lesion contrast. Please note that wave fields are displayed with the original matrix size of 80x80 pixels while stiffness maps are zoomed in to a central section of 40x40 pixels.

Figure 3 displays the error map calculated from the contrast difference between the reconstructed and true $|G^*|$ distribution. Contour lines indicate error levels. Error increased when stiffness of the inclusion increased, suggesting that both MDEV and

k-MDEV cannot retrieve correct values when inclusion stiffness is high. Negative stiffness contrast was better recovered than positive stiffness contrast, as demonstrated by relatively low error values (<30%) for soft inclusions. Nevertheless, k-MDEV tended to smooth out softer lesions, leading to larger error than MDEV, similar to the soft scenario shown in Figure 2. Overall, larger inclusions are better resolved.

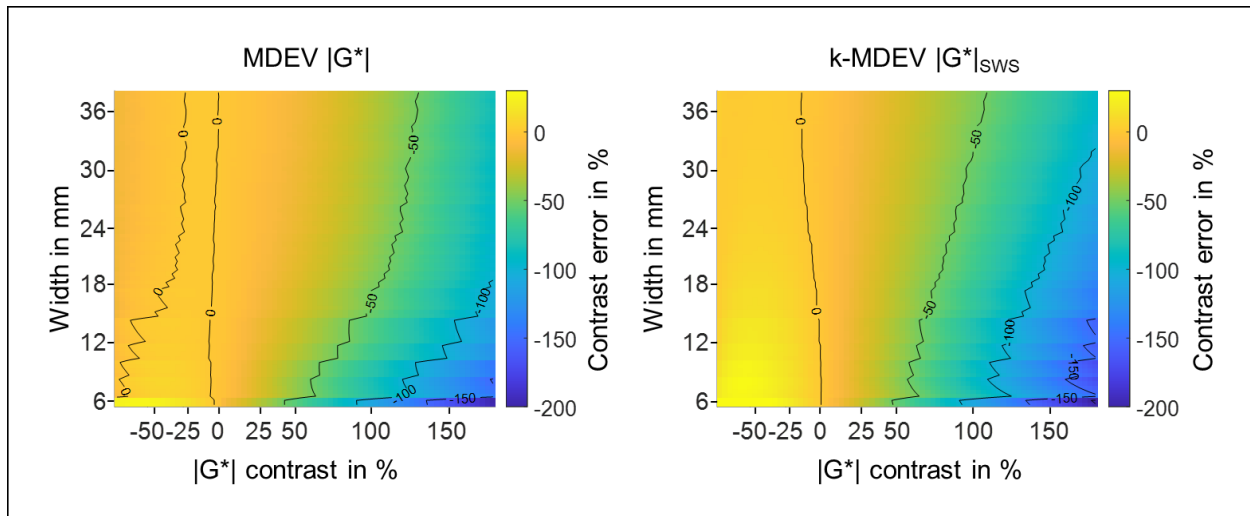


Figure 3: Stiffness contrast difference between true and reconstructed MDEV $|G^*|$ and k-MDEV $|G^*|_{SWS}$ distribution as an error map in relation to lesion width, which ranged from 6 to 38 mm (full-width-half-maximum of Gaussian-shaped lesion), and true $|G^*|$ contrast, which ranged from -80% to +180%. The color bar indicates the contrast error with respective error levels as contour lines. Error levels increase when lesions become smaller.

Reconstructed stiffness contrast over true stiffness contrast for two different lesion sizes is shown in Figure 4. 9-mm lesion diameter (full-width-half-maximum of Gaussian-shaped lesion) refers to the mean lesion diameter encountered in the in vivo experiments. 11.5 mm refers to the median size of the largest 25% of lesion diameters encountered in the in vivo experiments. Both reconstruction methods yielded spuriously low values for stiff inclusions due to noise-related artifact in finite-difference-based wave inversions. Consistent with Figure 3, MDEV performed better than k-MDEV for negative stiffness contrasts with low error (<10%). For MDEV inversion, an estimated contrast of $\pm 10\%$ was

reached when true contrast was +35% or -11% for stiff and soft lesions, respectively. For k-MDEV inversion, the delineation limit was reached at +57% or -25%.

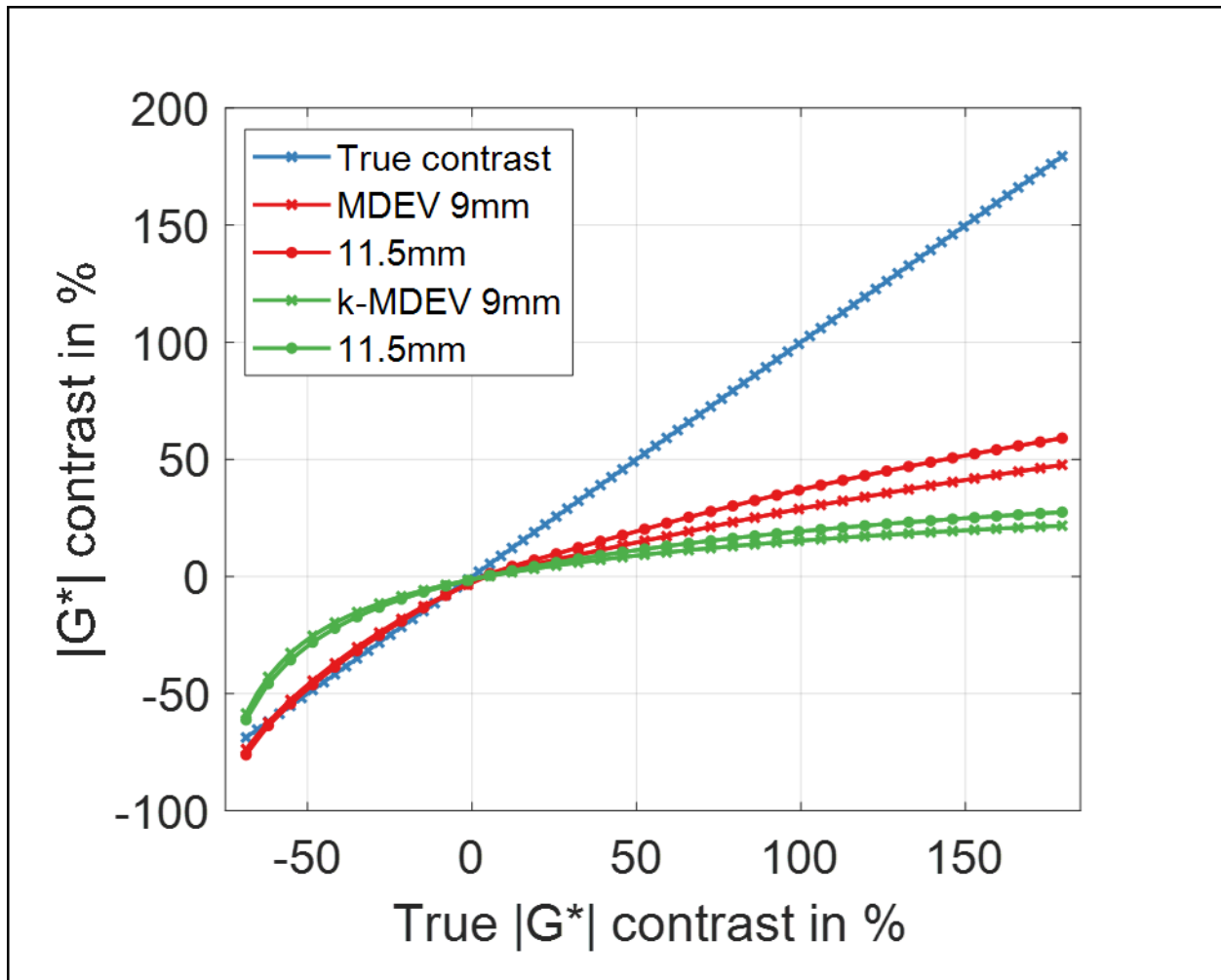


Figure 4: Reconstructed stiffness contrast of MDEV $|G^*|$ and k-MDEV $|G^*|_{\text{sws}}$ over true stiffness contrast for two different lesion sizes of 9 mm and 11.5 mm. The 9-mm lesion diameter (full-width-half-maximum of Gaussian-shaped lesion) refers to the mean lesion diameter encountered in the in vivo experiments. 11.5-mm refers to the median size of the largest 25% of lesion diameters encountered in the in vivo experiments

Phantom analysis

Figure 5 shows the results for the phantom analysis. The inclusions and ROIs for the inclusion masks are visible in the magnitude image. Inclusion numbers and ground-truth

$|G^*|$ contrasts are given as well. In addition, reconstructed $|G^*|$, $|G^*|_{\text{SWS}}$ and SWS maps are given for the central slice of the phantom. Displacement SNR of inclusion 1 was 15 ± 4 dB and therefore markedly lower than SNR of the matrix and the other inclusions (≈ 28 dB). Table 2 summarizes the phantom results.

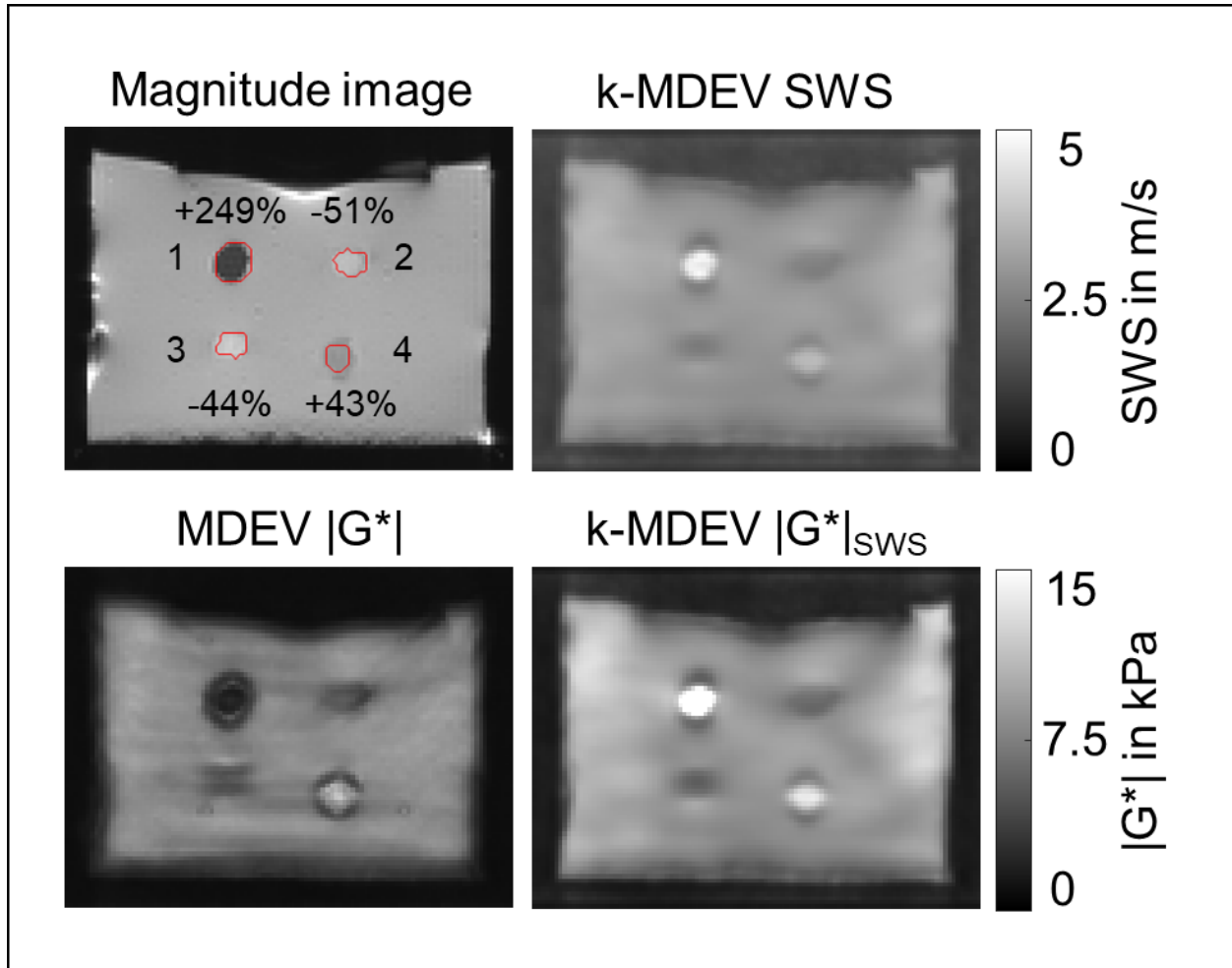


Figure 5: Results of the phantom experiment for one central slice. The top row shows the magnitude image and k-MDEV-reconstructed shear wave speed (SWS) map, together with the inclusions and ROIs for the inclusion masks. Inclusion numbers and ground-truth $|G^*|$ contrasts are given as well. The bottom row shows the MDEV $|G^*|$ and k-MDEV $|G^*|_{\text{SWS}}$ reconstructions.

Matrix stiffness was underestimated by 17% using MDEV while it was correctly retrieved by k-MDEV (only 1% deviation). MDEV was highly disturbed in inclusion 1, where noise

dominated second-order derivatives of large wavelengths [42], leading to spuriously soft properties. In contrast, k-MDEV, which invokes only first-order derivatives, detected stiff contrast in inclusion 1; however, still markedly underestimating true values (+125% versus +249%). In agreement with the wave simulation results, both MDEV and k-MDEV more precisely reconstructed soft than stiff inclusions. Unlike wave simulations, phantom inclusions considerably differed in displacement SNR. With increased agar gel concentration, SNR decreased. Hence, k-MDEV better reproduced focal stiffness changes, since MDEV values are typically more affected by noise [34, 42]. We choose lower frequencies to carefully balance between wave damping (increasing with frequency) and wave numbers (decreasing with frequency).

Differences between MDEV and k-MDEV were expected based on the finite-difference schemes used by the inversion method, which were of second and first order, respectively [42]. While our wave simulations favored MDEV, the phantom showed the potential strength of k-MDEV in lesion detection. Henceforth, both inversion strategies were applied to in vivo data.

In vivo experiments

A total of 147 lesions were manually segmented. The average number of lesions per patient was 12 (standard deviation [SD]: 5, range 7 - 22). The average size per lesion was 0.38 cm³ (SD: 0.40 cm³, range 0.03 – 2.6 cm³), which gives an average diameter of 9 mm assuming a spherical shape. The average surrounding tissue size was 0.85 cm³ (SD: 0.55 cm³). Per-patient results are provided in Table 1.

The exclusion of MS lesions (Figure 1, black arrow), CSF (Figure 1, white arrow), and solid-fluid boundaries from control masks led to a smaller average size of the control regions of 0.31 cm³ (SD: 0.30 cm³, range 0.03 – 1.5 cm³). Although the size difference between MS lesions and control regions was significant ($p < 0.001$), the effect size was small (Cohen's d of 0.4), and no correlation of lesion size with stiffness contrast was found ($p^* > 0.99$).

Typical wave images of a patient are shown in Figure 6 for all driving frequencies and encoding directions. Due to the dominant lateral motion induced by alternating phases of the compressed-air drivers, in-plane wave components showed higher wave amplitudes than through-plane wave components. Wave amplitudes decreased with frequency. Averaged displacement SNR in NAWM was 29 ± 3 dB.

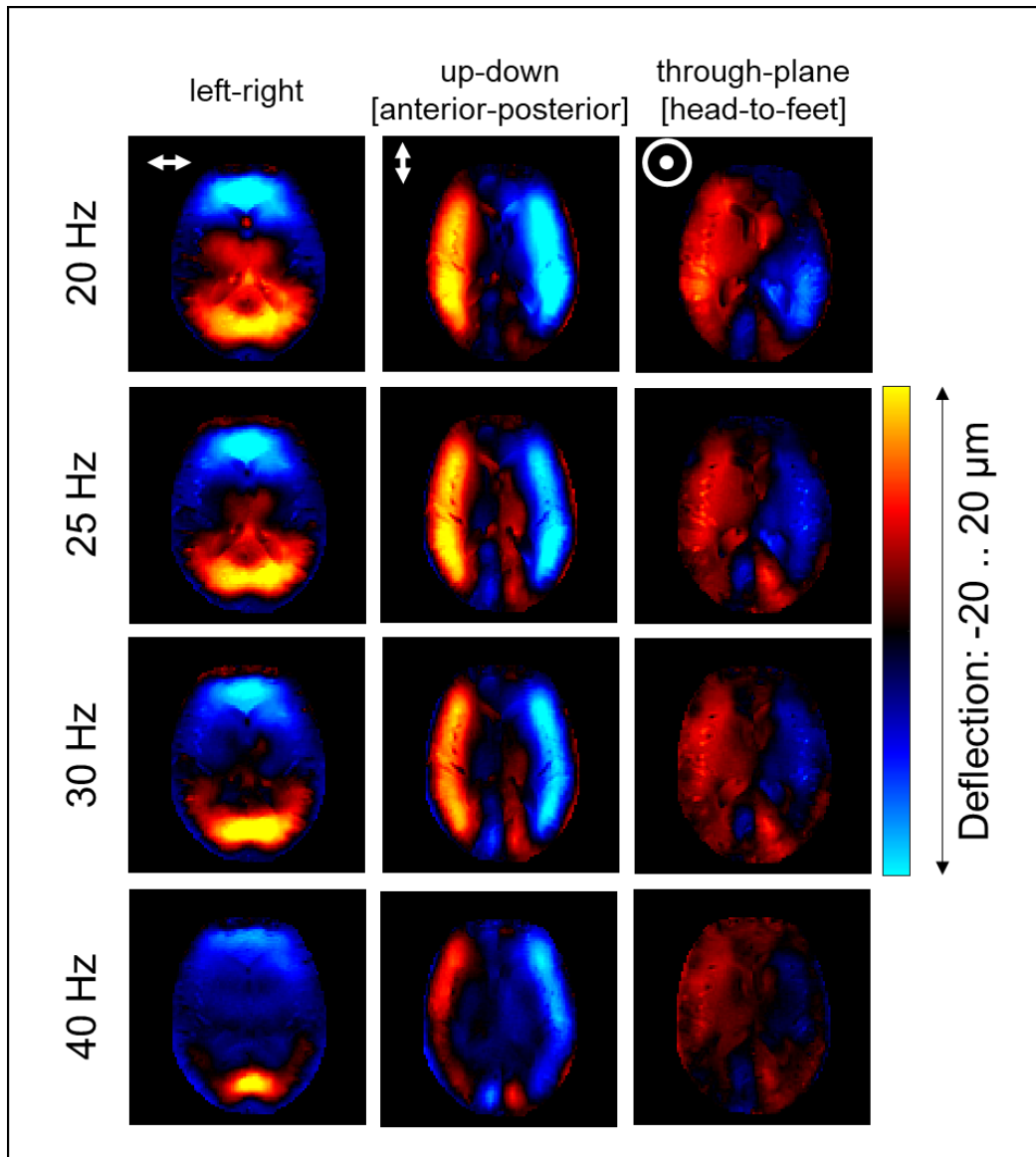


Figure 6: Real part of complex wave images of one patient for a central slice. All driving frequencies (20, 25, 30 and 40 Hz) and encoding directions are shown (↔ , ↑↓ , ⊙ denote deflections left-right, up-down [anterior-posterior] and through-plane [head-to-feet],

respectively). In-plane wave components show higher wave amplitudes than through-plane wave components. Wave amplitudes decrease with frequency.

Figure 7 shows representative slices of T2- weighted FLAIR-MRI, $|G^*|$, SWS and $|G^*|_{SWS}$ for three patients. Lesion masks are demarcated by red lines while the surrounding tissue masks are shown in green. The lesions appear hyperintense in the T2- weighted images. Lesions were not visible in MDEV and k-MDEV maps.

NAWM group mean $|G^*|$ and $|G^*|_{SWS}$ were 934 ± 82 Pa and 1922 ± 82 Pa with intra-regional standard deviations of 267 ± 46 Pa and 428 ± 41 Pa. The different values result from different noise responses, known as inversion bias of k-MDEV and MDEV[42].

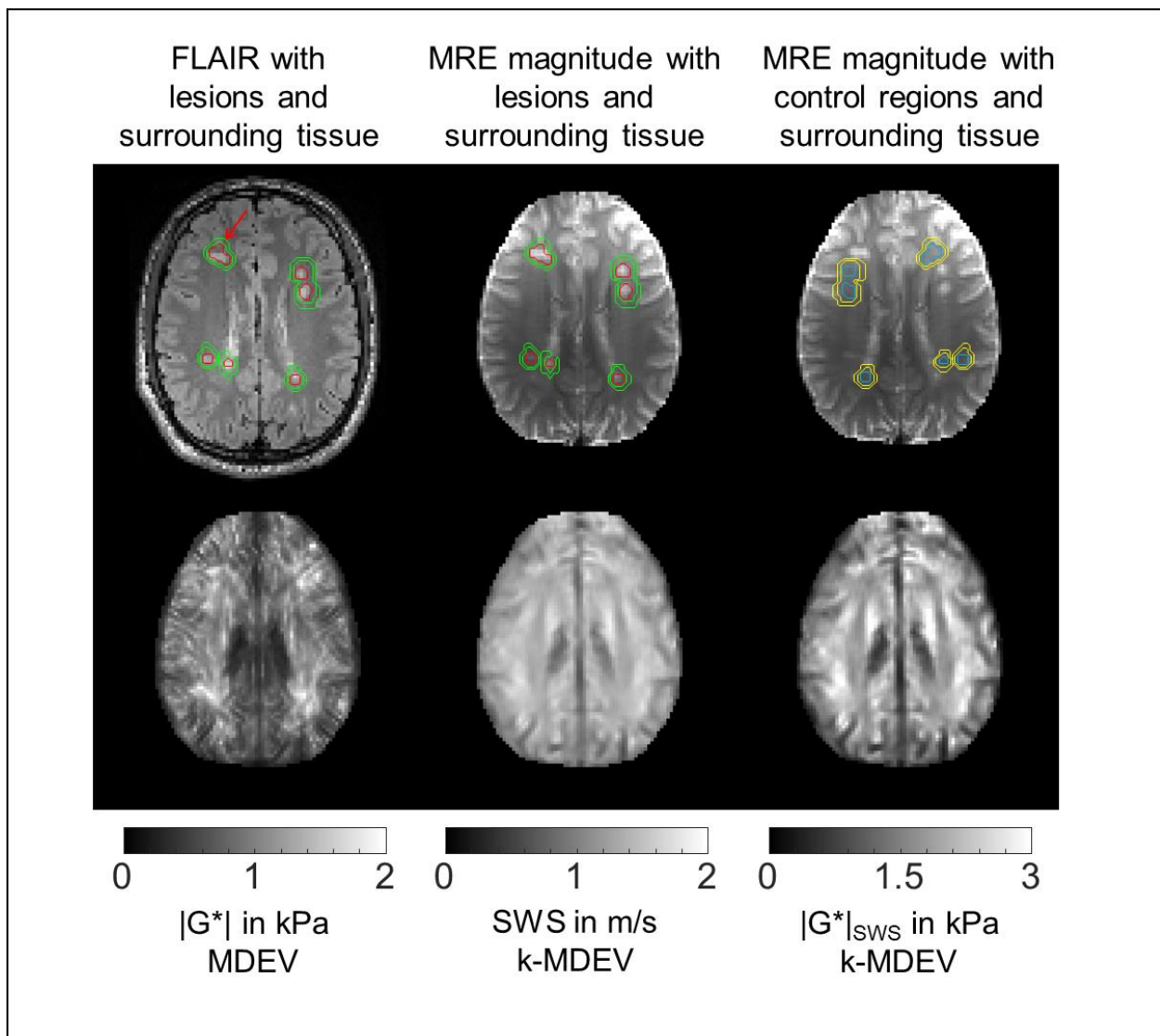


Figure 7: Representative slices of co-registered T2-weighted FLAIR-MRI images, MRE mean magnitude images, MDEV $|G^*|$, k-MDEV SWS and k-MDEV $|G^*|_{\text{SWS}}$ maps for one patient. Lesion masks are demarcated by red lines while the surrounding tissue masks are shown in green. Control regions are demarcated in blue and their surrounding tissue in yellow. Lesions appear hyperintense in T2-weighted images while they are not visible in MDEV and k-MDEV maps. A slight registration mismatch between FLAIR and mean MRE magnitude images is visible in some of the lesions (e.g., red arrow). All masks were generated using mean MRE magnitude images and the corresponding parameter maps, in which stiffness contrast was analyzed.

Figure 8 presents the distribution of stiffness contrast of MS lesions (contrast C1), control regions (contrast C2), and stiffness contrast between MS lesions versus control regions (contrast C3).

Figure 8a shows results of $|G^*|$ contrast obtained by MDEV. Mean values were similar for C1 ($2.1 \pm 11.2\%$), C2 ($1.8 \pm 11.6\%$), and C3 ($1.3 \pm 18.4\%$) with $p = 0.86$. C1 significantly differed from zero ($p = 0.02$) while C2 ($p = 0.06$) and C3 ($p = 0.13$) did not. A total of 80 MS lesions were stiffer while 67 were softer than their surrounding tissue. Thirty-five stiff lesions and 17 soft lesions exceeded the theoretical delineation limit. Yet, a similar pattern was observed for control regions (76 stiffer, 71 softer), indicating that this apparent stiffness contrast falls into the range of normal WM heterogeneity. Thirty-one stiff control regions and 20 soft control regions exceeded the theoretical delineation limit.

Figure 8b shows results of $|G^*|_{\text{SWS}}$ contrast obtained by k-MDEV. Again, similar distributions were obtained for C1 ($-2.2 \pm 10.4\%$), C2 ($-0.8 \pm 9.1\%$), and C3 ($-1.8 \pm 16.0\%$) with $p = 0.80$. Again, C1 significantly differed from zero ($p = 0.004$) while C2 ($p = 0.17$) and C3 ($p = 0.70$) did not. A total of 56 MS lesions were stiffer and 91 were softer than surrounding tissue. Twenty stiff lesions and 30 soft lesions exceeded the theoretical delineation limit. In the contralateral brain, 60 lesions were stiffer and 87 were softer; and 17 stiff control regions and 20 soft control regions exceeded the theoretical delineation limit.

Figure 8c illustrates delineation of MS lesions by $T2_{int}$ provided by FLAIR images. MS lesion intensity contrast was significantly ($p < 0.001$) higher (C1, $30.6 \pm 12.1\%$) than that of control regions (C2, $1.8 \pm 6.0\%$). A total of 146 lesions were hyperintense and 1 was hypointense while 86 control regions were hyperintense and 61 were hypointense. Lesion intensity was on average $30.7 \pm 15.0\%$ higher than control intensity in contralateral sites (C3, $p < 0.001$). Outliers in the histograms might be due to co-registration artifacts between MRE-derived masks and FLAIR images. No correlations were observed between C1 and lesion SNR ($p^* > 0.99$), lesion size ($p^* > 0.99$), and CSF proximity ($p^* = 0.09$).

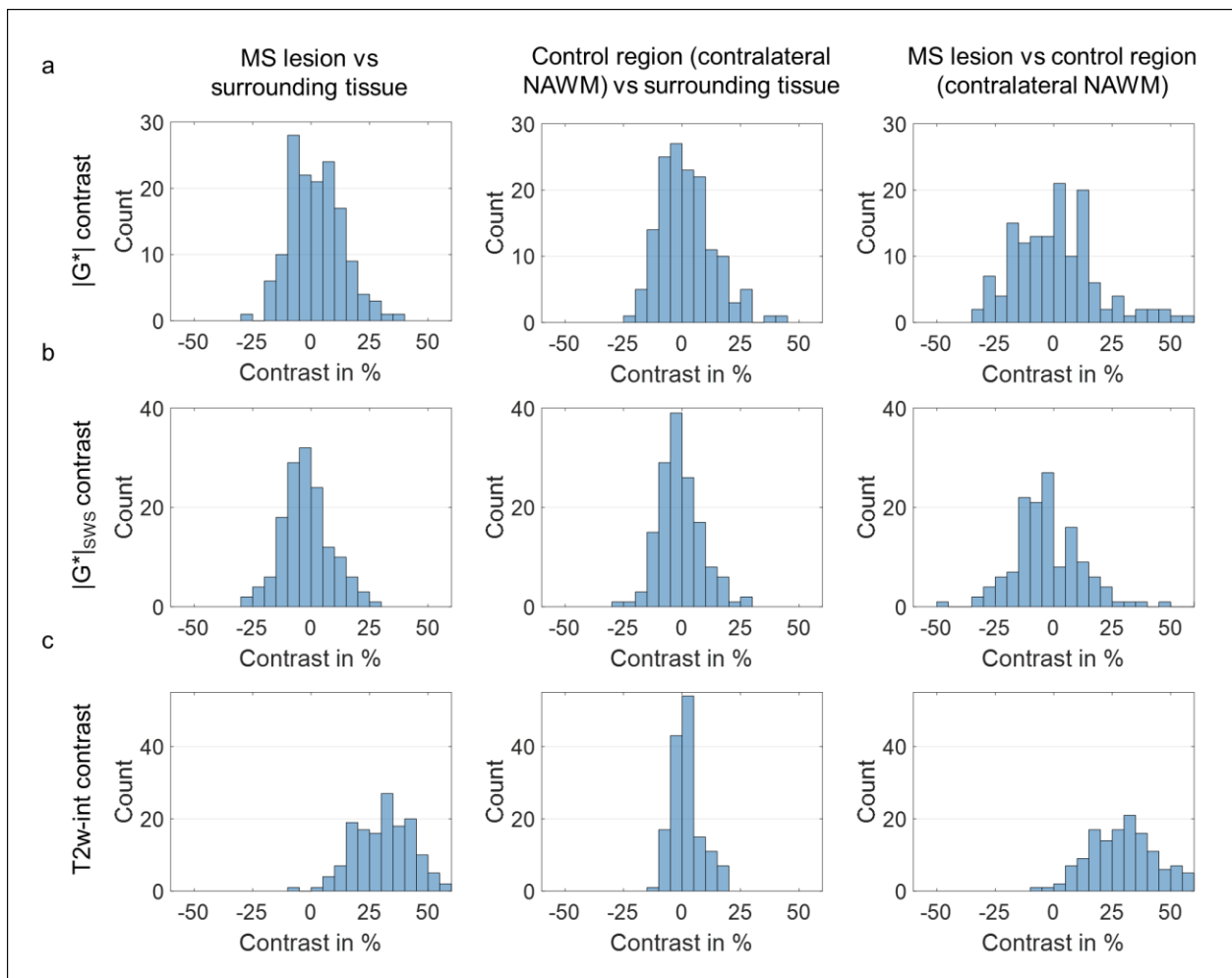


Figure 8: Distribution of different contrast values for MS lesions versus surrounding tissue (C1, left), control regions in the contralateral brain versus surrounding tissue (C2, middle), and MS lesions versus control regions (C3, right). **(a)** $|G^*|$ contrast distributions in MDEV.

(b) $|G^*|_{SWS}$ contrast distributions in k-MDEV. **(c)** $T2_{int}$ contrast distributions in T2-weighted FLAIR images.

Discussion

To the best of our knowledge, this is the first systematic analysis of imaging contrast generated by MRE in MS lesions that accounts for the current delineation limit of MRE in NAWM. Previous work investigating MS lesion detection used regional analysis and interpreted mean values at the site of the lesion without consideration of similar patterns in control regions in NAWM [23]. However, human brain tissue is highly heterogeneous, resulting in a wide variability of MRE values. Consequently, MRE parameter maps often appear very heterogeneous, making it challenging to identify smaller lesions by eye. Therefore, we automatically processed lesion masks by accounting for (i) the relative intensity difference between lesion and surrounding tissue (contrast), (ii) signal changes due to heterogeneous MRE values in contralateral control regions and (iii) MRE intensity differences between MS and control regions. This strategy allowed us (i) to observe that 54% and 46% of all analyzed lesions are stiffer and softer compared with surrounding tissue using MDEV inversion, respectively, and (ii) that a similar pattern is observed when looking at arbitrary regions throughout the brain. While (i) alone might suggest systematic variation due to a possible diversity of pathologic states of MS lesions, (ii) shows that there is no evidence for such a systematic pattern. While 35% of the lesions exceeded the visual delineation limit of 10%, none was apparent to the eye compared to the contralateral site. The symmetry of brain hemispheres is typically used as a criterion for the detection of focal brain abnormalities in addition to the contrast provided by surrounding tissue [55, 56]. However, the symmetry of brain MRE maps is frequently compromised by the presence of hotspots, which are often due to wave scattering at tissue boundaries and pose another challenge for lesion detection based on WM stiffness.

Overall our NAWM values fall into the range of previously reported stiffness values acquired by in vivo MRE [6, 7, 37]. Slightly lower $|G^*|$ mean values (933 vs 1412 Pa in Hetzer *et al.* [7]) are expected based on previous reports of symptomatic softening of brain tissue by MS [16, 57, 58]. Furthermore, the range of vibration frequencies used in this study

(20 to 40 Hz) was slightly lower than that of other studies (50 or 60 Hz) [12, 59] yielding an expected reduction of stiffness due to viscoelastic dispersion [35]. Also, our $|G^*|_{\text{sWS}}$ values fall within the range of previously reported values [35, 59] and are in agreement with single-frequency estimates of brain stiffness (2230 Pa for a center frequency of 28.5 Hz in [35]). In general, $|G^*|_{\text{sWS}}$ is higher than $|G^*|$ and better matches ground-truth values as demonstrated by the phantom experiments. This can be explained by the more severe inversion bias in direct inversion, which relies on second-order derivatives (MDEV), compared with phase-gradient methods, which use only first-order derivatives (k-MDEV) [34, 42]. Nevertheless, MDEV inversion is more established in brain MRE than k-MDEV as it does not involve directional filters. Such filters potentially bias the curvature of shear waves and affect wave numbers near interfaces more severely than second-order derivative operators. Therefore, we here analyzed MDEV and k-MDEV and found that both methods favored the detection of soft inclusions. However, it should be mentioned that this observation is specific to wavenumbers, noise, and discretization in our simulations. As described in Mura *et al.*, the requirements for minimum inversion bias are more relaxed for k-MDEV than for MDEV, but both depend on SNR and spatial support[42]. As a rule of thumb, a wavelength should be discretized by at least eight pixels, and at least half of the wavelength should be visible within the region of interest[60]. These conditions seem to be better fulfilled in our scenarios of softer and larger lesions, while stiffer and smaller lesions result in more severe inversion bias.

Stiffness of glial cells possibly influences the potential of remyelination of neurons in demyelinated lesions[2]. This was demonstrated by *ex vivo* experiments using atomic force and scanning force microscopy together with histology on a cellular level in tissue specimens [61-63]. The observed stiffness differences in MS lesions are probably driven by changes in glial reactivity and composition of the extracellular matrix (ECM) as they might not be explained by altered myelin content alone [2]. It has been shown that accumulation of reactive astrocytes and fibronectin dominates ECM remodeling in chronic lesions and might explain their sclerotic, i.e., stiffening behavior [61, 64]. By contrast, inflammation with gliosis during demyelination has been reported to be associated with tissue softening at lesion sites[63], partially because glial cells have been measured softer

than neurons [65]. Consistently, glial scars have recently been shown to be softer than normal CNS tissue [3], although they were previously thought to be stiffer [3, 61].

Our study shows that these microscopic stiffness changes do not result in marked changes in macroscopic stiffness contrast, which becomes visually apparent for contrasts larger than 10%. The magnitudes of stiffness contrasts in our study were similar to the overall reduction in brain stiffness in the order of approximately 15 – 20% in patients with MS[16], making the apparent effect of MS lesions relatively minor. Also, compared to other diseases such as prostate tumors, where tissue stiffening has been reported on the order of 140% in prostate cancer and still 40% in benign prostatic hyperplasia [66], MRE does not show similarly marked changes in MS lesions.

We consider the majority of all lesions investigated in our study to be chronic in nature. Since all patients in our cohort were on immunomodulatory treatment, disease progression was slowed down, the latest relapses occurred months before MRE and examinations were performed when the patients were fully asymptomatic. Although we cannot rule out the existence of fresh, acute (and possibly soft [2]) lesions, we consider them as rare, so that our results predominantly reflect properties of chronic (possibly stiff) lesions. As shown by simulations, contrast of stiff lesions is largely underestimated. Furthermore, smaller lesions tend to be masked by mechanical heterogeneities such as slip tissue boundaries. In our study, most lesions were located in periventricular areas, where tissue-to-fluid boundaries impose special challenges to MRE reconstruction algorithms if local homogeneity is assumed [29]. Otherwise, even larger lesions do not show consistent patterns of stiffness contrast, suggesting that mechanical changes are subtle and well below our proposed delineation limit.

Our study has limitations. First, it was not possible to determine lesion activity since invasive gadolinium-based contrast agent (GBCA)-enhanced MRI scans were not granted by the ethics committee, which are helpful to identify the activity state of MS lesions. Reports on gadolinium retention in brain tissue has raised concerns among clinicians and authorities and led to a ban of GBCA for follow-up examinations and imaging studies in our institution [21, 67, 68]. Second, the number of study participants

was relatively small. However, MS lesions can exhibit different characteristics even in the same patient, yielding a relatively high number of 147 delineated lesions in our study cohort and thus providing sufficient statistical power to analyze the delineation limit of MRE in MS lesions. Third, the spatial resolution of our imaging technique was not the highest that has been achieved in brain MRE thus far. Previous work by our groups was performed with 1 mm³ voxel size, however, in a 7-Tesla experimental MRI scanner [33]. Johnson and co-workers achieved 1.25 x 1.25 x 1.25 mm³ voxel size in a clinical 3-Tesla scanner [69], which might improve the delineation of smaller MS lesions. However, preliminary data acquired with slightly higher in-plane resolution (1.5 x 1.5 x 2 mm³) in 8 patients with MS in our institution did not show significant stiffness changes in focal areas associated with MS lesions [24]. Furthermore, even larger lesions, e.g., 0.8 cm³ covered by more than 100 voxels, were not visible with the methods used here, indicating that image resolution was not the critical parameter in our study. Yet, it should be mentioned that high image resolution is just one parameter that supports high-resolution stiffness mapping while multiple other parameters of the inversion pipeline such as kernel sizes, and smoothing thresholds determine the point-spread function of MRE. We focused here on 2D inversion methods as they have been proven useful for the detection of neurological diseases by MRE [14, 15, 70, 71]. Moreover our 3D technique suffered from boundary artefacts along the head-foot (slice select) direction which distorted up to six edge slices at the borders. Nevertheless we tested if 3D inversion changed our key results and applied the full inversion pipeline based on 3D k-MDEV to all data of this study. 3D k-MDEV [72] applied to the 3D curl field (instead of high-pass filtered wave fields) showed no different results than those presented here. However, it is expected that technical advances in MRE with respect to drivers, imaging sequences [73-75] and inversion strategies [29, 30, 76, 77] will enable in vivo stiffness-based characterization of MS lesions in the future. To encourage these developments our data will be made available upon request.

In summary, we systematically analyzed local stiffness properties of MS lesions compared to NAWM in a cohort of patients with relapsing-remitting MS. Based on our data, Charcot's assumption that MS is a focal sclerotic disease can neither be dismissed

nor confirmed for in vivo tissue. Nevertheless, our results show that the stiffness variations occurring in MS lesions are within the normal range of WM heterogeneity and below the variation induced by other diseases such as tumors. The facts that brain tissue softens in MS and that MS lesions are not markedly altered in stiffness suggest that marked tissue sclerosis may not be a mechanical signature of MS.

Acknowledgments

Funding from the German Research Foundation (GRK 2260 BIOQIC, SFB1340 Matrix in Vision, Sa901/17-2) is gratefully acknowledged. Moreover, we would like to thank Susan Pikol and Cynthia Kraut from the Experimental and Clinical Research Center at Charité Berlin for their support in conducting the MRI examinations.

Declaration of conflicting interests

The authors declare no potential conflicts of interest with respect to the research, authorship, and publication of this article.

Author contributions

HH as first author performed the formal analysis, developed the methodology, analyzed the data for validation and visualization and wrote the original draft as well as the review and any editing of the manuscript. SH supported the investigation, data validation and funding acquisition. MS and FP contributed to the data curation, funding acquisition and assisted in the formal analysis with regard to medical characteristics of the disease. MSh assisted in interpreting the results with regard to medical characteristics and supported the statistical analysis. JB helped supervise the project and acquire funding and constructed the actuation system. IS conceptualized and supervised the project, performed funding acquisition, aided in the formal analysis and interpretation of the results and wrote the original draft of the manuscript.

All authors provided critical feedback, contributed to the methodology and the original draft of the manuscript.

Tables

Table 1. Patient data including number and size of segmented MS lesions. In addition, MDEV $|G^*|$ and k-MDEV $|G^*|_{\text{SWS}}$ average values and standard deviations or ranges in brackets for all lesions, surrounding tissue and NAWM. NAWM averaged and mean lesion displacement SNR in dB is given as well.

| No | Age | Sex | Month since disease onset | Month since last relapse | Numb. of lesions | MS lesion size in cm ³ | Surrounding tissue size in cm ³ | NAWM $ G^* $ in Pa | NAWM $ G^* _{\text{SWS}}$ in Pa | NAWM SNR in dB | Mean MS lesion SNR in dB |
|----|-----|-----|---------------------------|--------------------------|------------------|-----------------------------------|--|--------------------|---------------------------------|----------------|--------------------------|
| 1 | 52 | F | 168 | 59 | 12 | 0.27 (0.04-1.19) | 0.57 (0.24-1.13) | 811 (197) | 1803 (371) | 27 (4) | 34 (26-42) |
| 2 | 36 | F | 124 | 23 | 13 | 0.25 (0.04-0.46) | 0.62 (0.18-1.03) | 927 (260) | 1917 (394) | 26 (3) | 35 (31-41) |
| 3 | 54 | M | 141 | 31 | 7 | 0.27 (0.11-0.53) | 0.77 (0.38-1.36) | 919 (253) | 1947 (436) | 28 (5) | 36 (32-42) |
| 4 | 25 | M | 32 | 2 | 10 | 0.57 (0.27-1.08) | 1.26 (0.85-1.91) | 972 (258) | 1986 (483) | 29 (4) | 37 (30-42) |
| 5 | 34 | M | 5 | 5 | 15 | 0.35 (0.06-1.58) | 0.93 (0.50-2.74) | 971 (280) | 2007 (432) | 31 (6) | 37 (31-44) |
| 6 | 56 | M | 175 | 102 | 12 | 0.29 (0.03-1.42) | 0.72 (0.28-1.93) | 832 (204) | 1772 (361) | 25 (5) | 33 (26-41) |
| 7 | 62 | F | 364 | 51 | 12 | 0.88 (0.09-2.60) | 1.11 (0.55-2.23) | 862 (248) | 1895 (445) | 29 (5) | 37 (34-42) |
| 8 | 52 | M | 68 | 21 | 9 | 0.29 (0.05-0.37) | 0.69 (0.41-0.98) | 954 (283) | 1918 (444) | 31 (4) | 40 (36-44) |
| 9 | 37 | M | 127 | 17 | 8 | 0.25 (0.06-0.34) | 0.68 (0.44-1.00) | 1052 (335) | 2056 (475) | 35 (5) | 42 (35-48) |

| | | | | | | | | | | | |
|--------------|--------------------------|---|----------------------------|--------------------------|-------------------------|------------------------------|------------------------------|---------------------------|----------------------------|-------------------------|-------------------------|
| 10 | 44 | M | 160 | 70 | 22 | 0.38 (0.06-1.24) | 0.78 (0.34-1.80) | 862 (256) | 1861 (384) | 28 (3) | 36 (26-44) |
| 11 | 22 | F | 267 | 36 | 8 | 0.21 (0.06-0.66) | 0.70 (0.42-1.29) | 963 (276) | 1978 (437) | 33 (5) | 44 (40-51) |
| 12 | 60 | F | 469 | 289 | 19 | 0.50 (0.06-1.59) | 1.10 (0.39-2.50) | 1077 (358) | 1922 (470) | 26 (4) | 31 (26-35) |
| MEAN (SD) | 45 (14) | | 175 (134) | 56 (78) | 12 (5) | 0.38 (0.19) | 0.83 (0.22) | 933 (82) | 1922 (82) | 29 (3) | 37 (4) |

Table 2. Phantom results. Displacement SNR, MDEV-based $|G^*|$ and k-MDEV-based $|G^*|_{SWS}$ average values and standard deviations in brackets for the gel matrix and four inclusions, together with resulting contrasts for one central slice.

| | Displacement SNR in dB mean (SD) | Ground-truth $ G^* $ | | MDEV $ G^* $ | | kMDEV $ G^* _{SWS}$ | |
|--------|----------------------------------|----------------------|---------------|--------------------------|-------------------------|--------------------------------|-------------------------|
| | | $ G^* $ in kPa | Contrast in % | $ G^* $ in kPa mean (SD) | Contrast in % mean (SD) | $ G^* _{SWS}$ in kPa mean (SD) | Contrast in % mean (SD) |
| Matrix | 27 (2) | 10.1 | - | 8.4 (0.5) | - | 10.0 (1.1) | |
| in 1 | 15 (4) | 35.3 | +249 | 2.7 (0.9) | -70 (9) | 22.7 (1.7) | +125 (16) |
| in 2 | 27 (2) | 4.9 | -51 | 4.6 (0.6) | -46 (9) | 6.3 (0.1) | -38 (1) |
| in 3 | 29 (5) | 5.6 | -44 | 4.9 (0.3) | -42 (2) | 5.7 (0.3) | -43 (3) |
| in 4 | 28 (5) | 14.4 | +43 | 10 (1.0) | +19 (8) | 13.5 (0.4) | +35 (4) |

References

- [1] B. Zalc, One hundred and fifty years ago Charcot reported multiple sclerosis as a new neurological disease, *Brain* 141(12) (2018) 3482-3488.
- [2] M.M. Urbanski, M.B. Brendel, C.V. Melendez-Vasquez, Acute and chronic demyelinated CNS lesions exhibit opposite elastic properties, *Sci Rep* 9(1) (2019) 999.
- [3] E. Moeendarbary, I.P. Weber, G.K. Sheridan, D.E. Koser, S. Soleman, B. Haenzi, E.J. Bradbury, J. Fawcett, K. Franze, The soft mechanical signature of glial scars in the central nervous system, *Nat Commun* 8 (2017) 14787.
- [4] A.A. de Schellenberger, H. Tzschätzsch, B. Polchlopek, G. Bertalan, F. Schrank, K. Garczynska, P.A. Janmey, J. Braun, I. Sack, Sensitivity of multifrequency magnetic resonance elastography and diffusion-weighted imaging to cellular and stromal integrity of liver tissue, *J Biomech* 88 (2019) 201-208.
- [5] G. Bertalan, P. Boehm-Sturm, S. Schreyer, A.S. Morr, B. Steiner, H. Tzschätzsch, J. Braun, J. Guo, I. Sack, The influence of body temperature on tissue stiffness, blood perfusion, and water diffusion in the mouse brain, *Acta Biomater* 96 (2019) 412-420.
- [6] S. Hetzer, P. Birr, A. Fehlner, S. Hirsch, F. Dittmann, E. Barnhill, J. Braun, I. Sack, Perfusion alters stiffness of deep gray matter, *J Cereb Blood Flow Metab* 38(1) (2018) 116-125.
- [7] S. Hetzer, F. Dittmann, K. Bormann, S. Hirsch, A. Lipp, D.J. Wang, J. Braun, I. Sack, Hypercapnia increases brain viscoelasticity, *J Cereb Blood Flow Metab* 39(12) (2019) 2445-2455.
- [8] B. Kreft, H. Tzschätzsch, F. Schrank, J. Bergs, K.-J. Streitberger, S. Wäldchen, S. Hetzer, J. Braun, I. Sack, Time-Resolved Response of Cerebral Stiffness to Hypercapnia in Humans, *Ultrasound in medicine & biology* 46(4) (2020) 936-943.
- [9] J. Weickenmeier, M. Kurt, E. Ozkaya, R. de Rooij, T.C. Ovaert, R.L. Ehman, K. Butts Pauly, E. Kuhl, Brain stiffens post mortem, *J Mech Behav Biomed Mater* 84 (2018) 88-98.
- [10] G. Bertalan, C. Klein, S. Schreyer, B. Steiner, B. Kreft, H. Tzschätzsch, A.A. de Schellenberger, M. Nieminen-Kelha, J. Braun, J. Guo, I. Sack, Biomechanical properties of the hypoxic and dying brain quantified by magnetic resonance elastography, *Acta Biomater* 101 (2020) 395-402.

- [11] S. Hirsch, J. Braun, I. Sack, *Magnetic Resonance Elastography: Physical Background And Medical Applications*, Wiley-VCH2017.
- [12] L.V. Hiscox, C.L. Johnson, E. Barnhill, M.D. McGarry, J. Huston, E.J. van Beek, J.M. Starr, N. Roberts, *Magnetic resonance elastography (MRE) of the human brain: technique, findings and clinical applications*, *Phys Med Biol* 61(24) (2016) R401-R437.
- [13] Z. Yin, A.J. Romano, A. Manduca, R.L. Ehman, J. Huston, 3rd, *Stiffness and Beyond: What MR Elastography Can Tell Us About Brain Structure and Function Under Physiologic and Pathologic Conditions*, *Top Magn Reson Imaging* 27(5) (2018) 305-318.
- [14] J. Wuerfel, F. Paul, B. Beierbach, U. Hamhaber, D. Klatt, S. Papazoglou, F. Zipp, P. Martus, J. Braun, I. Sack, *MR-elastography reveals degradation of tissue integrity in multiple sclerosis*, *Neuroimage* 49(3) (2010) 2520-5.
- [15] A. Fehlner, J.R. Behrens, K.J. Streitberger, S. Papazoglou, J. Braun, J. Bellmann-Strobl, K. Ruprecht, F. Paul, J. Wurfel, I. Sack, *Higher-resolution MR elastography reveals early mechanical signatures of neuroinflammation in patients with clinically isolated syndrome*, *J Magn Reson Imaging* 44(1) (2016) 51-8.
- [16] K.J. Streitberger, I. Sack, D. Krefting, C. Pfuller, J. Braun, F. Paul, J. Wuerfel, *Brain viscoelasticity alteration in chronic-progressive multiple sclerosis*, *PLoS One* 7(1) (2012) e29888.
- [17] K.J. Streitberger, A. Fehlner, F. Pache, A. Lacheta, S. Papazoglou, J. Bellmann-Strobl, K. Ruprecht, A. Brandt, J. Braun, I. Sack, F. Paul, J. Wuerfel, *Multifrequency magnetic resonance elastography of the brain reveals tissue degeneration in neuromyelitis optica spectrum disorder*, *Eur Radiol* 27(5) (2017) 2206-2215.
- [18] K. Schregel, E. Wuerfel, P. Garteiser, I. Gemeinhardt, T. Prozorovski, O. Aktas, H. Merz, D. Petersen, J. Wuerfel, R. Sinkus, *Demyelination reduces brain parenchymal stiffness quantified in vivo by magnetic resonance elastography*, *Proc Natl Acad Sci U S A* 109(17) (2012) 6650-5.
- [19] J.M. Millward, J. Guo, D. Berndt, J. Braun, I. Sack, C. Infante-Duarte, *Tissue structure and inflammatory processes shape viscoelastic properties of the mouse brain*, *NMR Biomed* 28(7) (2015) 831-9.
- [20] K. Riek, J.M. Millward, I. Hamann, S. Mueller, C.F. Pfueller, F. Paul, J. Braun, C. Infante-Duarte, I. Sack, *Magnetic resonance elastography reveals altered brain*

viscoelasticity in experimental autoimmune encephalomyelitis, *Neuroimage Clin* 1(1) (2012) 81-90.

[21] S. Wang, J.M. Millward, L. Hanke-Vela, B. Malla, K. Pilch, A. Gil-Infante, S. Waiczies, S. Mueller, P. Boehm-Sturm, J. Guo, I. Sack, C. Infante-Duarte, MR Elastography-Based Assessment of Matrix Remodeling at Lesion Sites Associated With Clinical Severity in a Model of Multiple Sclerosis, *Front Neurol* 10 (2019) 1382.

[22] R.V. Silva, A.S. Morr, S. Mueller, S.P. Koch, P. Boehm-Sturm, Y. Rodriguez-Sillke, D. Kunkel, H. Tzschätzsch, A.A. Kuhl, J. Schnorr, M. Taupitz, I. Sack, C. Infante-Duarte, Contribution of Tissue Inflammation and Blood-Brain Barrier Disruption to Brain Softening in a Mouse Model of Multiple Sclerosis, *Front Neurosci* 15 (2021) 701308.

[23] C.L. Johnson, C.A. Thompson, B.M. Sandroff, T.A. Edwards, E.A. Hubbard, R.E. Klaren, H. Schwarb, B.P. Sutton, L.A. Pilutti, R.W. Motl, Multiple sclerosis lesions are softer than surrounding white matter: An MR elastography study, in: *I.P.o.t.s.A.M.o. ISMRM (Ed.) Proc 25st Annual Meeting ISMRM*, 2017.

[24] H. Herthum, S. Hetzer, M. Scheel, F. Paul, H. Tzschätzsch, T. Meyer, M. Shahryari, J. Braun, I. Sack, Are multiple sclerosis lesions stiffer or softer than surrounding brain tissue?, in: *I.P.o.t.s.A.M.o. ISMRM (Ed.) ISMRM & SMRT Virtual Conference & Exhibition*, 2021.

[25] P. Sun, A. George, D.C. Perantie, K. Trinkaus, Z. Ye, R.T. Naismith, S.K. Song, A.H. Cross, Diffusion basis spectrum imaging provides insights into MS pathology, *Neurol Neuroimmunol Neuroinflamm* 7(2) (2020).

[26] C.L. Johnson, M.D. McGarry, A.A. Gharibans, J.B. Weaver, K.D. Paulsen, H. Wang, W.C. Olivero, B.P. Sutton, J.G. Georgiadis, Local mechanical properties of white matter structures in the human brain, *Neuroimage* 79 (2013) 145-52.

[27] M.C. Murphy, J. Huston, 3rd, C.R. Jack, Jr., K.J. Glaser, M.L. Senjem, J. Chen, A. Manduca, J.P. Felmlee, R.L. Ehman, Measuring the characteristic topography of brain stiffness with magnetic resonance elastography, *PLoS One* 8(12) (2013) e81668.

[28] J. Guo, S. Hirsch, A. Fehlner, S. Papazoglou, M. Scheel, J. Braun, I. Sack, Towards an elastographic atlas of brain anatomy, *PLoS One* 8(8) (2013) e71807.

- [29] E. Barnhill, P.J. Davies, C. Ariyurek, A. Fehlnner, J. Braun, I. Sack, Heterogeneous Multifrequency Direct Inversion (HMDI) for magnetic resonance elastography with application to a clinical brain exam, *Med Image Anal* 46 (2018) 180-188.
- [30] L.M. Solamen, M.D. McGarry, L. Tan, J.B. Weaver, K.D. Paulsen, Phantom evaluations of nonlinear inversion MR elastography, *Phys Med Biol* 63(14) (2018) 145021.
- [31] M.M. Doyley, J.B. Weaver, E.E. Van Houten, F.E. Kennedy, K.D. Paulsen, Thresholds for detecting and characterizing focal lesions using steady-state MR elastography, *Med Phys* 30(4) (2003) 495-504.
- [32] M. Honarvar, R. Rohling, S.E. Salcudean, A comparison of direct and iterative finite element inversion techniques in dynamic elastography, *Phys Med Biol* 61(8) (2016) 3026-48.
- [33] J. Braun, J. Guo, R. Lutzkendorf, J. Stadler, S. Papazoglou, S. Hirsch, I. Sack, J. Bernarding, High-resolution mechanical imaging of the human brain by three-dimensional multifrequency magnetic resonance elastography at 7T, *Neuroimage* 90 (2014) 308-314.
- [34] H. Tzschatzsch, J. Guo, F. Dittmann, S. Hirsch, E. Barnhill, K. Johrens, J. Braun, I. Sack, Tomoelastography by multifrequency wave number recovery from time-harmonic propagating shear waves, *Med Image Anal* 30 (2016) 1-10.
- [35] H. Herthum, S.C.H. Dempsey, A. Samani, F. Schrank, M. Shahryari, C. Warmuth, H. Tzschatzsch, J. Braun, I. Sack, Superviscous properties of the in vivo brain at large scales, *Acta Biomater* 121 (2021) 393-404.
- [36] F. Schrank, C. Warmuth, H. Tzschatzsch, B. Kreft, S. Hirsch, J. Braun, T. Elgeti, I. Sack, Cardiac-gated steady-state multifrequency magnetic resonance elastography of the brain: Effect of cerebral arterial pulsation on brain viscoelasticity, *J Cereb Blood Flow Metab* 40(5) (2020) 991-1001.
- [37] F. Dittmann, S. Hirsch, H. Tzschatzsch, J. Guo, J. Braun, I. Sack, In vivo wideband multifrequency MR elastography of the human brain and liver, *Magn Reson Med* 76(4) (2016) 1116-26.
- [38] Z. Yin, Y. Sui, J.D. Trzasko, P.J. Rossman, A. Manduca, R.L. Ehman, J. Huston, 3rd, In vivo characterization of 3D skull and brain motion during dynamic head vibration using magnetic resonance elastography, *Magn Reson Med* 80(6) (2018) 2573-2585.

- [39] W.D. Penny, K.J. Friston, J.T. Ashburner, S.J. Kiebel, T.E. Nichols, Statistical parametric mapping: the analysis of functional brain images, Elsevier 2011.
- [40] P.A. Yushkevich, J. Piven, H.C. Hazlett, R.G. Smith, S. Ho, J.C. Gee, G. Gerig, User-guided 3D active contour segmentation of anatomical structures: Significantly improved efficiency and reliability, *Neuroimage* 31(3) (2006) 1116-1128.
- [41] S. Papazoglou, S. Hirsch, J. Braun, I. Sack, Multifrequency inversion in magnetic resonance elastography, *Phys Med Biol* 57(8) (2012) 2329-46.
- [42] J. Mura, F. Schrank, I. Sack, An analytical solution to the dispersion-by-inversion problem in magnetic resonance elastography, *Magn Reson Med* 84(1) (2020) 61-71.
- [43] S.R. Marticorena Garcia, M. Grossmann, A. Bruns, M. Durr, H. Tzschätzsch, B. Hamm, J. Braun, I. Sack, J. Guo, Tomoelastography Paired With T2* Magnetic Resonance Imaging Detects Lupus Nephritis With Normal Renal Function, *Invest Radiol* 54(2) (2019) 89-97.
- [44] S.R. Marticorena Garcia, L. Zhu, E. Gultekin, R. Schmuck, C. Burkhardt, M. Bahra, D. Geisel, M. Shahryari, J. Braun, B. Hamm, Z.Y. Jin, I. Sack, J. Guo, Tomoelastography for Measurement of Tumor Volume Related to Tissue Stiffness in Pancreatic Ductal Adenocarcinomas, *Invest Radiol* 55(12) (2020) 769-774.
- [45] R. Reiter, H. Tzschätzsch, F. Schwahofer, M. Haas, C. Bayerl, M. Muche, D. Klatt, S. Majumdar, M. Uyanik, B. Hamm, J. Braun, I. Sack, P. Asbach, Diagnostic performance of tomoelastography of the liver and spleen for staging hepatic fibrosis, *Eur Radiol* 30(3) (2020) 1719-1729.
- [46] T. Meyer, H. Tzschätzsch, J. Braun, P. Kalra, A. Kolipaka, I. Sack, Online platform for extendable server-based processing of magnetic resonance elastography data., in: I.P.o.t.s.A.M.o. ISMRM (Ed.) Proc 23st Annual Meeting ISMRM, Montreal, 2019, p. 3966.
- [47] K.J. Streitberger, L. Lilaj, F. Schrank, J. Braun, K.T. Hoffmann, M. Reiss-Zimmermann, J.A. Kas, I. Sack, How tissue fluidity influences brain tumor progression, *Proc Natl Acad Sci U S A* 117(1) (2020) 128-134.
- [48] K.J. Streitberger, M. Reiss-Zimmermann, F.B. Freimann, S. Bayerl, J. Guo, F. Arlt, J. Wuerfel, J. Braun, K.T. Hoffmann, I. Sack, High-resolution mechanical imaging of glioblastoma by multifrequency magnetic resonance elastography, *PLoS One* 9(10) (2014) e110588.

- [49] M. Shahryari, T. Meyer, C. Warmuth, H. Herthum, G. Bertalan, H. Tzschatzsch, L. Stencel, S. Lukas, L. Lilaj, J. Braun, I. Sack, Reduction of breathing artifacts in multifrequency magnetic resonance elastography of the abdomen, *Magn Reson Med* 85(4) (2021) 1962-1973.
- [50] H. Herthum, M. Shahryari, H. Tzschatzsch, F. Schrank, C. Warmuth, S. Gorner, S. Hetzer, H. Neubauer, J. Pfeuffer, J. Braun, I. Sack, Real-Time Multifrequency MR Elastography of the Human Brain Reveals Rapid Changes in Viscoelasticity in Response to the Valsalva Maneuver, *Front Bioeng Biotechnol* 9(335) (2021) 666456.
- [51] D.L. Donoho, I.M. Johnstone, G. Kerkycharian, D. Picard, Wavelet shrinkage: asymptopia?, *Journal of the Royal Statistical Society: Series B (Methodological)* 57(2) (1995) 301-337.
- [52] G. Bertalan, J. Guo, H. Tzschatzsch, C. Klein, E. Barnhill, I. Sack, J. Braun, Fast tomoelastography of the mouse brain by multifrequency single-shot MR elastography, *Magn Reson Med* 81(4) (2019) 2676-2687.
- [53] F. Schrank, C. Warmuth, S. Gorner, T. Meyer, H. Tzschatzsch, J. Guo, Y.O. Uca, T. Elgeti, J. Braun, I. Sack, Real-time MR elastography for viscoelasticity quantification in skeletal muscle during dynamic exercises, *Magn Reson Med* 84(1) (2020) 103-114.
- [54] E. Barnhill, L. Hollis, I. Sack, J. Braun, P.R. Hoskins, P. Pankaj, C. Brown, E.J.R. van Beek, N. Roberts, Nonlinear multiscale regularisation in MR elastography: Towards fine feature mapping, *Med Image Anal* 35 (2017) 133-145.
- [55] S.X. Liu, Symmetry and asymmetry analysis and its implications to computer-aided diagnosis: A review of the literature, *J Biomed Inform* 42(6) (2009) 1056-64.
- [56] M.J. van Putten, The revised brain symmetry index, *Clin Neurophysiol* 118(11) (2007) 2362-7.
- [57] A. Arani, M.C. Murphy, K.J. Glaser, A. Manduca, D.S. Lake, S.A. Kruse, C.R. Jack, Jr., R.L. Ehman, J. Huston, 3rd, Measuring the effects of aging and sex on regional brain stiffness with MR elastography in healthy older adults, *Neuroimage* 111 (2015) 59-64.
- [58] M.C. Murphy, J. Huston, 3rd, R.L. Ehman, MR elastography of the brain and its application in neurological diseases, *Neuroimage* 187 (2019) 176-183.
- [59] L.V. Hiscox, M.D.J. McGarry, H. Schwarb, E.E.W. Van Houten, R.T. Pohlig, N. Roberts, G.R. Huesmann, A.Z. Burzynska, B.P. Sutton, C.H. Hillman, A.F. Kramer, N.J.

- Cohen, A.K. Barbey, K.D. Paulsen, C.L. Johnson, Standard-space atlas of the viscoelastic properties of the human brain, *Hum Brain Mapp* 41(18) (2020) 5282-5300.
- [60] S. Papazoglou, U. Hamhaber, J. Braun, I. Sack, Algebraic Helmholtz inversion in planar magnetic resonance elastography, *Phys Med Biol* 53(12) (2008) 3147-58.
- [61] Y.B. Lu, K. Franze, G. Seifert, C. Steinhauser, F. Kirchhoff, H. Wolburg, J. Guck, P. Janmey, E.Q. Wei, J. Kas, A. Reichenbach, Viscoelastic properties of individual glial cells and neurons in the CNS, *Proc Natl Acad Sci U S A* 103(47) (2006) 17759-64.
- [62] Y.B. Lu, I. Iandiev, M. Hollborn, N. Korber, E. Ulbricht, P.G. Hirrlinger, T. Pannicke, E.Q. Wei, A. Bringmann, H. Wolburg, U. Wilhelmsson, M. Pekny, P. Wiedemann, A. Reichenbach, J.A. Kas, Reactive glial cells: increased stiffness correlates with increased intermediate filament expression, *FASEB J* 25(2) (2011) 624-31.
- [63] D. Eberle, G. Fodolianaki, T. Kurth, A. Jagielska, S. Möllmert, E. Ulbricht, K. Wagner, A.V. Taubenberger, N. Träber, J.-C. Escolano, K.J. Van Vliet, J. Guck, Acquired demyelination but not genetic developmental defects in myelination leads to brain tissue stiffness changes, *Brain Multiphysics* 1 (2020) 100019.
- [64] J.M. Stoffels, J.C. de Jonge, M. Stancic, A. Nomden, M.E. van Strien, D. Ma, Z. Siskova, O. Maier, C. French-Constant, R.J. Franklin, D. Hoekstra, C. Zhao, W. Baron, Fibronectin aggregation in multiple sclerosis lesions impairs remyelination, *Brain* 136(Pt 1) (2013) 116-31.
- [65] K. Franze, P.A. Janmey, J. Guck, Mechanics in neuronal development and repair, *Annu Rev Biomed Eng* 15 (2013) 227-51.
- [66] M. Li, J. Guo, P. Hu, H. Jiang, J. Chen, J. Hu, P. Asbach, I. Sack, W. Li, Tomoelastography Based on Multifrequency MR Elastography for Prostate Cancer Detection: Comparison with Multiparametric MRI, *Radiology* 299(2) (2021) 362-370.
- [67] A.H. El-Khatib, H. Radbruch, S. Trog, B. Neumann, F. Paul, A. Koch, M.W. Linscheid, N. Jakubowski, E. Schellenberger, Gadolinium in human brain sections and colocalization with other elements, *Neurol Neuroimmunol Neuroinflamm* 6(1) (2019) e515.
- [68] L. Schlemm, C. Chien, J. Bellmann-Strobl, J. Dorr, J. Wuerfel, A.U. Brandt, F. Paul, M. Scheel, Gadopentetate but not gadobutrol accumulates in the dentate nucleus of multiple sclerosis patients, *Mult Scler* 23(7) (2017) 963-972.

- [69] P.L. Delgorio, L.V. Hiscox, A.M. Daugherty, F. Sanjana, R.T. Pohlig, J.M. Ellison, C.R. Martens, H. Schwarb, M.D.J. McGarry, C.L. Johnson, Effect of Aging on the Viscoelastic Properties of Hippocampal Subfields Assessed with High-Resolution MR Elastography, *Cereb Cortex* 31(6) (2021) 2799-2811.
- [70] K.J. Streitberger, E. Wiener, J. Hoffmann, F.B. Freimann, D. Klatt, J. Braun, K. Lin, J. McLaughlin, C. Sprung, R. Klingebiel, I. Sack, In vivo viscoelastic properties of the brain in normal pressure hydrocephalus, *NMR Biomed* 24(4) (2011) 385-92.
- [71] L.M. Gerischer, A. Fehlner, T. Kobe, K. Prehn, D. Antonenko, U. Grittner, J. Braun, I. Sack, A. Floel, Combining viscoelasticity, diffusivity and volume of the hippocampus for the diagnosis of Alzheimer's disease based on magnetic resonance imaging, *Neuroimage Clin* 18 (2018) 485-493.
- [72] H. Herthum, H. Tzschätzsch, T. Meyer, M. Shahryari, L. Stencel, J. Guo, J. Braun, I. Sack, Magnetic resonance elastography of the in vivo human brain using multifrequency wavenumber analysis in 2D and 3D., in: I.P.o.t.s.A.M.o. ISMRM (Ed.) ISMRM & SMRT Virtual Conference & Exhibition, 2021.
- [73] W. Majeed, P. Kalra, A. Kolipaka, Simultaneous multislice rapid magnetic resonance elastography of the liver, *NMR Biomed* 33(4) (2020) e4252.
- [74] J. Strasser, M.T. Haindl, R. Stollberger, F. Fazekas, S. Ropele, Magnetic resonance elastography of the human brain using a multiphase DENSE acquisition, *Magn Reson Med* 81(6) (2019) 3578-3587.
- [75] Y. Sui, A. Arani, J.D. Trzasko, M.C. Murphy, P.J. Rossman, K.J. Glaser, K.P. McGee, A. Manduca, R.L. Ehman, P.A. Araoz, J. Huston, 3rd, TURBINE-MRE: A 3D hybrid radial-Cartesian EPI acquisition for MR elastography, *Magn Reson Med* 85(2) (2021) 945-952.
- [76] J.M. Scott, A. Arani, A. Manduca, K.P. McGee, J.D. Trzasko, J. Huston, 3rd, R.L. Ehman, M.C. Murphy, Artificial neural networks for magnetic resonance elastography stiffness estimation in inhomogeneous materials, *Med Image Anal* 63 (2020) 101710.
- [77] D. Fovargue, S. Kozerke, R. Sinkus, D. Nordsletten, Robust MR elastography stiffness quantification using a localized divergence free finite element reconstruction, *Med Image Anal* 44 (2018) 126-142.